The recovery of polymer melts after shear and elongational flows

Ulrik Borgbjerg and Juan José de Pablo
Department of Chemical Engineering, University of Wisconsin Madison, Madison, Wisconsin 53706

Hans Christian Öttinger
Institut für Polymere, Eidgenossische Technische Hochschule, ETH-Zentrum, CH-8092 Zürich, Switzerland

(Received 7 February 1994; accepted 8 July 1994)

This work examines the constrained recoil after steady shear flow and the free recovery after steady elongational flow of monodisperse polymer melts. Calculations are performed in the framework of the Curtiss–Bird theory using both conventional numerical integrations and nonequilibrium Brownian dynamics. The latter approach is shown to have significant advantages, particularly at high shear or elongational rates. The predicted curves of recovery as a function of shear rate exhibit an unusual maximum for which several explanations are proposed.

INTRODUCTION

Non-Newtonian fluids such as polymer melts or dilute polymer solutions are said to have memory. If a non-Newtonian fluid has been subject to a shearing force for some time and this force is suddenly removed, the fluid flows backwards, or recovers. This flow pattern is termed "recovery" or "recoil"; such behavior is analogous to a rubber band snapping back when released after stretching. On the microscopic level, polymer molecules are stretched by the external force. When this force is removed, the molecules contract. Modeling these flows not only provides useful knowledge for practical applications, but also serves as a stringent test for the model itself. Flows involving recoil possess a high order of complexity, since they are unsteady and involve behavior on a variety of time scales.

Modeling polymer melts is important for various reasons. Models provide a wide range of information valuable in industry, such as velocity profiles, pressure drops, viscosity functions, and diffusion coefficients. Several models for polymer melts have been proposed in the past. These can be broadly classified into two categories: network theories[1] and reptation theories.[2–4] In network theories, the melt is modeled as a network of chains joined at junctions. Reptation theories assume that single chains adopt particular conformations in response to an average field imposed by the surrounding molecules. The Curtiss–Bird model (CBM),[3] used throughout this paper, falls within the latter category. In such a model, an anisotropic friction tensor leads to preferential motion of the chains along their backbones.

The CBM was selected for this study because it has shown to be capable of describing many different material functions for several simple elongational and shear flows for both monodisperse and polydisperse melts.[5–8] In their original studies of their model, Curtiss, Bird, and their co-workers examined simple shear and elongational flows; so far, constrained recoil after steady shear flow and free recovery after steady elongational flow have not been investigated. Experimental data for these flows are scarce and, to the best of our knowledge, attempts to model them have been limited.

This paper examines the ultimate recoil of monodisperse polymer melts after simple steady shear flows and after simple steady elongational flows. For shear flows, the mathematical equations in the theory are solved using two different methods. The first is a conventional numerical method, in which the relevant integrals are solved directly. The second relies on a stochastic approach which has been proven to be particularly useful in earlier work with non-Newtonian fluids.[9–12] The stochastic calculations can be regarded as Brownian dynamics simulations of the CBM. For reasons that will become apparent later, in the case of elongational flows, we are particularly interested in investigating the high-elongational-rate regime; since for such a regime conventional numerical calculations become delicate, only the stochastic approach is employed.

We begin this paper with a formal description of the two unsteady recovery flows considered here followed by a brief overview of the CBM. We then discuss the two mathematical methods of solution employed in our work. Next, we present and discuss the actual predictions for the viscosity functions and the ultimate recovery for both flows. The paper is then concluded with several general remarks about the findings reported throughout this work.

FLOW FIELD

We consider two different unsteady flows, namely constrained recoil after steady shear flow and free recovery after steady elongational flow. Each flow comprises two stages. In the first stage, the fluid flows steadily. The stress is then removed at once and the fluid recovers to some previously occupied position. During recovery after shear flow, the distance between the walls is fixed and assumed to be small.

The velocity field for steady shear flow is $v_x=\dot{\gamma}_0 y$, $v_y=0$, and $v_z=0$, where $\dot{\gamma}_0$ is the shear rate. During the second stage of the flow, i.e., during recovery after $t=t_0$, a linear velocity profile is assumed and the xy component of the stress tensor τ_{xy} is set equal to 0;[13,14] the flow field therefore becomes time dependent and its velocity has components $v_x=\dot{\gamma}(t)y$, $v_y=0$, and $v_z=0$. Figure 1 illustrates $\dot{\gamma}$, γ, and τ_{xy} as a function of time for a typical recoil calculation. The ultimate recoil after shear flow is determined from

$$\gamma_\infty=\lim_{t\to\infty}\gamma_r(t), \tag{1a}$$

where

 0021-9606/94/101(8)/7144/10/$6.00

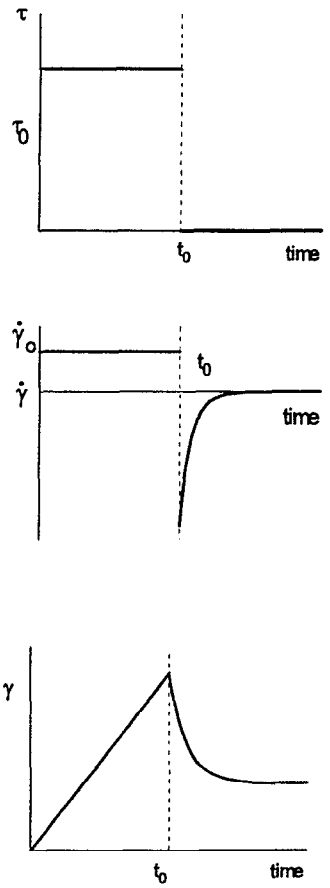

FIG. 1. A schematic representation of $\dot{\gamma}$, γ, and τ_{xy} during a recoil calculation (Ref. 13).

$$\gamma_r(t)=\int_{t=t_0}^{t}\dot{\gamma}(t')dt'. \tag{1b}$$

For simple elongational flow, the steady state velocity field has components $v_x=-\frac{1}{2}\dot{\epsilon}_0 x$, $v_y=-\frac{1}{2}\dot{\epsilon}_0 y$, and $v_z=\dot{\epsilon}_0 z$, where $\dot{\epsilon}_0$ is the elongational rate. For this flow, the only viscosity function of interest is the elongational viscosity defined by $\bar{\eta}=-(\tau_{zz}-\tau_{xx})/\dot{\epsilon}$. Recovery begins at $t=t_0$; the stress is suddenly removed and $\tau_{zz}-\tau_{xx}$ is set equal to 0. During recovery, we assume that the velocity field has components $v_x=-\frac{1}{2}\dot{\epsilon}(t)x$, $v_y=-\frac{1}{2}\dot{\epsilon}(t)y$, and $v_z=\dot{\epsilon}(t)z$.[14] The ultimate recoil after simple elongational flow is then calculated according to

$$\epsilon_\infty=\lim_{t\to\infty}\epsilon_r(t), \tag{2a}$$

where

$$\epsilon_r(t)=\int_{t=t_0}^{t}\dot{\epsilon}(t')dt'. \tag{2b}$$

THE CURTISS–BIRD MODEL

The Curtiss–Bird model (CBM) is based on a kinetic-theory development for Kramers' freely jointed bead–rod chains, where polymer molecules are modeled as N massless beads joined by $N-1$ freely rotating rigid links.[3]

Curtiss and Bird make four major approximations to arrive at a single link distribution function.[3] The first of these is the *short-range-force approximation*, which states that only beads very close to each other interact. The second is the use of an *anisotropic Stokes law*, which is an empirical, three-parameter equation for the hydrodynamic drag on a bead. One of the parameters in this law is the *link-tension coefficient* ϵ_l, which determines the anisotropy of the friction tensor. For $\epsilon_l=1$, the tensor is anisotropic, and for $\epsilon_l=0$, there is no difference between the forces acting on two succeeding beads in the direction of the link joining them. The theory of Curtiss and Bird reduces to that of Doi and Edwards[2] for $\epsilon_l=0$. The third approximation, known as the *anisotropic Brownian motion approximation*, states that, on average, the velocity of a bead relative to the center of mass velocity is in the direction of the chain. The polymer is therefore said to "reptate" through the melt. The fourth simplification, known as the *mild curvature approximation*, assumes that the chain approximates a curve with continuous derivatives (i.e., with no "kinks").

These approximations result in the following diffusion equation for the single link probability density $f(\mathbf{u},s,t)$ function:

$$\frac{\partial f}{\partial t}=\frac{1}{\lambda}\frac{\partial^2 f}{\partial s^2}-\frac{\partial}{\partial \mathbf{u}}\cdot(\kappa\cdot\mathbf{u}-\kappa:\mathbf{uuu})f, \tag{3}$$

where $f(\mathbf{u},s,t)$ is the time-dependent probability of finding a link at position s along the chain having orientation $\mathbf{u}$. By definition, s is a number between 0 and 1, and $\mathbf{u}$ is a unit vector. The time-dependent transposed velocity gradient tensor is denoted by κ, and λ is a characteristic time constant for the chains. For simplicity, throughout this paper, the value of λ has been set to unity. Note that besides the dependence of the distribution function, the first term in Eq. (3) depends only on the polymer properties and the second term depends only on the flow field.

The single link distribution function $f(\mathbf{u},s,t)$ is presumed to obey the following boundary conditions:

$$f(\mathbf{u},0,t)=f(\mathbf{u},1,t)=\frac{1}{4\pi}. \tag{4}$$

From a physical point of view, these conditions ensure that when a link of the polymer emerges from a chain, it points in all directions with equal probability.

Having developed expressions for the single link distribution function, Curtiss and Bird[3] determine the stress tensor τ according to

$$\tau=k_BTnN\left[\frac{1}{3}\,\delta-\langle\mathbf{uu}\rangle-\lambda\epsilon_l\kappa:\langle s(1-s)\mathbf{uuuu}\rangle\right], \tag{5}$$

where k_B is Boltzmann's constant, T is the temperature, n is the number density of beads, N is the number of beads in a chain, and δ is the unit tensor. For simplicity, the product

nNk_BT is set equal to unity. The brackets denote averages with respect to the probability function $f(\mathbf{u},s,t)$, e.g.,

$$\langle \mathbf{uu} \rangle = \int \int f(\mathbf{u},s,t)\mathbf{uu}\, ds\, d\mathbf{u} \tag{6}$$

and

$$\langle s(1-s)\mathbf{uuuu} \rangle = \int \int f(\mathbf{u},s,t)s(1-s)\mathbf{uuuu}\, ds\, d\mathbf{u}. \tag{7}$$

STOCHASTIC APPROACH

The stochastic approach proposed here relies on the transformation of a second order differential equation for a d-dimensional distribution function into a stochastic differential equation (SDE) for a d-dimensional process.[16,17] Consider a general diffusion equation of the form

$$\frac{\partial f}{\partial t} = -\frac{\partial}{\partial \mathbf{x}} \cdot [\mathbf{A}(\mathbf{x},t)f] + \frac{1}{2}\frac{\partial^2}{\partial \mathbf{x}^2} : [\mathbf{D}(\mathbf{x},t)f]. \tag{8}$$

Equation (8) can be shown to be equivalent to

$$d\mathbf{x} = \mathbf{A}dt + \mathbf{B}\cdot d\mathbf{W}, \quad \mathbf{D} = \mathbf{B}\cdot\mathbf{B}^T, \tag{9}$$

where $\mathbf{W}$ is a d-dimensional vector-valued Wiener process, $\mathbf{A}(\mathbf{x},t)$ is a d-dimensional vector, $\mathbf{B}(\mathbf{x},t)$ is a $d\times d'$ matrix, and $\mathbf{D}(\mathbf{x},t)$ is a positive-semidefinite symmetric $d\times d$ matrix. The solution to Eq. (8) is the distribution function $f(\mathbf{x},t)$ for the d-dimensional stochastic process $\mathbf{x}$ described by the SDE (9).

In our work $\mathbf{x}=(\mathbf{u},s)$; a transformation is carried out from the Curtiss–Bird diffusion equation

$$\frac{\partial f}{\partial t} = \frac{1}{\lambda}\frac{\partial^2 f}{\partial s^2} - \frac{\partial}{\partial \mathbf{u}} \cdot (\boldsymbol{\kappa}\cdot\mathbf{u} - \boldsymbol{\kappa}:\mathbf{uuu})f \tag{3}$$

to the following SDE:

$$\begin{cases} d\mathbf{u} = (\boldsymbol{\kappa}\cdot\mathbf{u} - \boldsymbol{\kappa}:\mathbf{uuu})dt & \text{(10a)} \\ ds = \sqrt{2/\lambda}\, dW. & \text{(10b)} \end{cases}$$

Equation (3) leads to a unidimensional process s and a three-dimensional process $\mathbf{u}$ whose only coupling is through the boundary conditions.

Care must be exercised when discretizing Eqs. (10a) and (10b) for a numerical solution. First we note that $\mathbf{u}$ is a unit vector; any discrete scheme to solve Eq. (10a) must therefore preserve this normalization. Second, it is important to point out that s is reflected whenever it reaches 0 or 1. Furthermore, when a reflection occurs, $\mathbf{u}$ is chosen randomly on a unit sphere; otherwise, $\mathbf{u}$ evolves independent of s.

In order to calculate the stress tensor (5), we need only average quantities determined from the distribution function. These values are found by simulating a large number of trajectories following Eqs. (10a) and (10b) and then taking an average over them.

The discretization of Eq. (10b) is remarkably simple.[16] For variable s, we use

$$s_{i+1} = s_i + \sqrt{\frac{2\Delta t}{\lambda}}\, W_i. \tag{11}$$

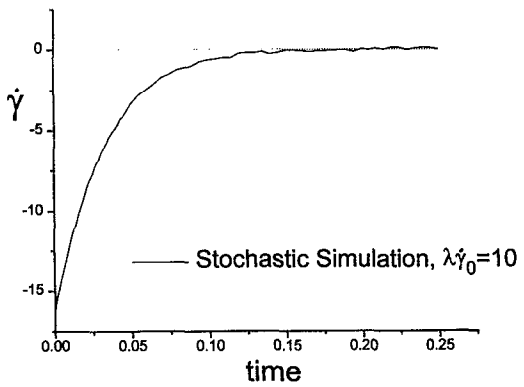

FIG. 2. Shear rate $\dot{\gamma}(t)$ during constrained recovery after shear flow. The line shows results of a stochastic simulation of 10^5 trajectories for $\lambda\dot{\gamma}_0=10$ and $\epsilon_l=0.1$.

The W_i's are independent random numbers generated from a Gaussian distribution with unit variance and zero mean. Due to the nature of the Wiener process,[17,18] s is reflected back into the interval [0,1] whenever it crosses 0 or 1 during a time step, i.e., $s_{r,i+1}=2B-s_{i+1}$, where B is either 0 or 1 depending on the boundary.

Equation (10b) is discretized into

$$\mathbf{u}_{i+1} = \mathbf{u}_i + (\boldsymbol{\kappa}\cdot\mathbf{u} - \boldsymbol{\kappa}:\mathbf{uuu})_i\Delta t \approx \frac{\mathbf{u}_i + \boldsymbol{\kappa}\cdot\mathbf{u}_i\Delta t}{|\mathbf{u}_i + \boldsymbol{\kappa}\cdot\mathbf{u}_i\Delta t|}, \tag{12}$$

where the normalization guarantees that the norm of $\mathbf{u}$ will be preserved. Note that Eq. (13) is only valid to order Δt.[19]

The time-dependent shear rate $\dot{\gamma}(t)$ during recovery [$\dot{\epsilon}(t)$ for elongational flows] can now be obtained for $t\geq t_0$ by following processes $\mathbf{u}$ and s as they evolve in time. Since the procedure for doing so is analogous for both shear flow and elongational flow, we only outline it for the former case.

A steady-state shear flow is first established for a constant shear rate $\dot{\gamma}_0$. During this stage, the xy component of the stress tensor is found from Eq. (5), i.e.,

$$\tau_{xy} = -\langle u_x u_y \rangle - \lambda\epsilon_l\dot{\gamma}_0\langle s(1-s)u_x^2u_y^2 \rangle. \tag{13}$$

Once τ_{xy} has reached its steady state value, the recoil experiment can begin. As indicated above, the shear rate $\dot{\gamma}(t)$ is now a function of time, but the xy component of the stress tensor is constant and is set equal to 0. The shear rate is therefore calculated at each time step according to

$$\dot{\gamma}(t) = -\frac{\langle u_x u_y \rangle}{\lambda\epsilon_l\langle s(1-s)u_x^2u_y^2 \rangle}. \tag{14}$$

Once $\dot{\gamma}(t)$ is known, the ultimate recoil can be calculated using Eq. (1). Figures 2 and 3 show $\dot{\gamma}(t)$ and $\gamma_r(t)$ for $t\geq t_0$ and $\lambda\dot{\gamma}_0=10$.

For elongational flows, the first viscosity function plays the role that τ_{xy} has for shear flows. From Eq. (5), we have

$$\tau_{zz} - \tau_{xx} = -[\langle u_z u_z \rangle - \langle u_x u_x \rangle] - \tfrac{1}{2}\dot{\epsilon}_0\epsilon_l\lambda[\langle s(1-s) \times (3u_z^4 - u_z^2) \rangle - \langle s(1-s)(3u_z^2-1)u_x^2 \rangle]. \tag{15}$$

The resulting expression for $\dot{\epsilon}(t)$ is now obtained by setting $\tau_{zz}-\tau_{xx}$ equal to zero; it is given by

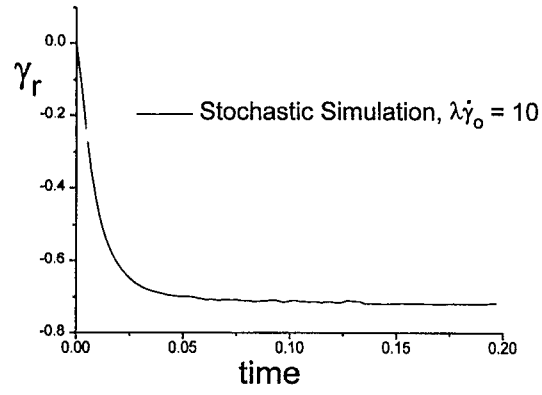

FIG. 3. Displacement $\gamma_r(t)$ during constrained recoil after shear flow. The line shows results of a stochastic simulation with 10^5 trajectories for $\lambda\dot{\gamma}_0=10$ and $\epsilon_i=0.1$.

$$\dot{\epsilon}(t) = -\frac{2[\langle u_z u_z\rangle - \langle u_x u_x\rangle]}{\lambda\epsilon_i[\langle s(1-s)(3u_z^4-u_z^2)\rangle - \langle s(1-s)(3u_z^2-1)u_x^2)\rangle]}. \tag{16}$$

We then determine $-\epsilon_\infty$, the ultimate recoil, from Eq. (2). Figures 4 and 5 show $\dot{\epsilon}(t)$ and $\epsilon_r(t)$ for $t \geqslant t_0$ and $\lambda\dot{\epsilon}_0=10$.

The main advantage of stochastic simulations (over conventional numerical integration techniques) resides in the fact that trajectories for $\mathbf{u}$ and s are generated according to the desired distribution function $f(\mathbf{u},s,t)$, thereby rendering the calculation of averages particularly simple. As discussed in the next section, the "conventional" method of solution requires the evaluation of memory integrals at each time step; such calculations can be highly computationally intensive, particularly at high shear rates.

At this point, there are several technicalities which must be addressed. Special problems arise when s is close to the ends of the interval [0,1]. In the remainder of this paper, such ends are called boundaries. Consider two successive time steps for which s_i and s_{i+1} are both within the allowed interval [0,1]. It is plausible that sometime between t_i and

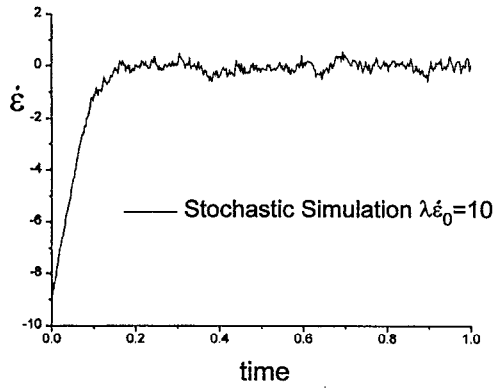

FIG. 4. Stochastic simulation with 10^4 trajectories of the elongational rate $\dot{\epsilon}(t)$ during free recovery after elongational flow for $\lambda\dot{\epsilon}_0=10$ and $\epsilon_i=0.3$.

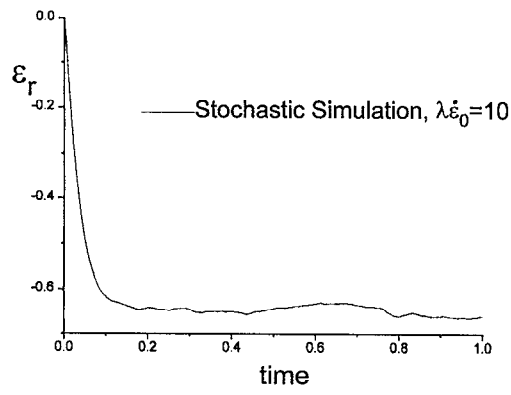

FIG. 5. Stochastic simulation with 10^4 trajectories of the displacement ϵ_r during free recovery after elongational flow for $\lambda\dot{\epsilon}_0=10$ and $\epsilon_i=0.3$.

$t_i+\Delta t$, process s could have left that interval and returned to it. We call such an event an overseen reflection. Note that these reflections would not affect s, but the corresponding unit vector $\mathbf{u}$ would be altered because the boundary conditions dictate that $\mathbf{u}$ must be chosen randomly whenever s is reflected.

The problem that we face is therefore that of determining whether any reflections occurred within a given time interval or not. Its solution is statistical in nature; the probability that one or more reflections occurred is calculated and compared to a random number R uniformly distributed on the interval [0,1]. The probability that at least one overseen reflection took place in the $(i+1)$th time step is given by[20]

$$P=\exp\left[-\frac{\lambda}{\Delta t}(B-s_i)(B-s_{i+1})\right], \tag{17}$$

where B is either 0 or 1, depending on which boundary is the nearest. If $P>R$, an overseen reflection is assumed to have occurred; if $P<R$, it is assumed that no overseen reflections took place.

When an overseen reflection occurs (i.e., when $P>R$), or also when a real reflection occurs, in which case $s_{i+1}\notin[0,1]$, the last reflection time is determined by a bisection procedure (see the Appendix). With such a procedure, the stochastic calculations lead to errors of order Δt.[10] To estimate the value of the ultimate recoil in the limit of zero time step, we conduct several simulations for the same conditions, but using different time steps. Figure 6 illustrates our estimation method: $-\gamma_\infty$ is shown for different values of Δt, and the extrapolation to zero time step is made by means of a linear regression.

A recoil calculation requires simulation of 10^4 to 10^5 trajectories, depending on the shear rate and on the desired level of accuracy. A calculation with 10^4 trajectories is achieved in a few hours of CPU time on a HP-RISC 730 workstation.

CONVENTIONAL NUMERICAL METHOD

The "conventional" numerical procedure we follow here to solve the recoil problem was actually inspired by the stochastic algorithm; it therefore bears some resemblance to the method described in the previous section. The problem is

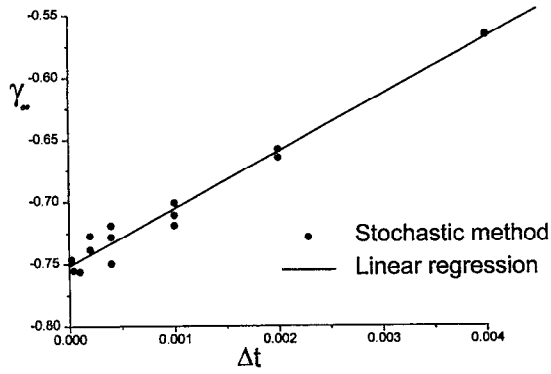

FIG. 6. Extrapolation of results of stochastic simulations of constrained recoil after shear flow to zero time step. The symbols represent simulations using different time steps. The line is obtained through a linear regression. $\lambda\dot{\gamma}_0=10$ and $\epsilon_l=0.1$.

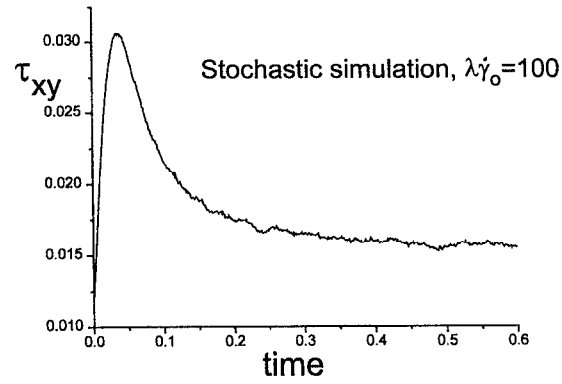

FIG. 7. Results of a stochastic simulation of the stress tensor after inception of shear flow for $\lambda\dot{\gamma}_0=100$ and $\epsilon_l=0.1$.

again divided into two stages. In the first stage, the shear rate is constant and τ_{xy} varies until a steady state is attained. In the second stage, the xy component of the stress tensor τ_{xy} is zero; $\dot{\gamma}(t)$ is then determined from Eq. (14). The difference with the stochastic approach resides in the fact that the averages appearing in that equation require a numerical evaluation of the corresponding "memory integrals."

The stress tensor is determined according to[3]

$$\tau=k_BTnN\left[\frac{1}{3}\,\delta-\int_\infty^t\mu(t-t')\mathbf{A}^{(2)}(t,t')dt'\right.$$
$$\left.-\epsilon_l\lambda\kappa:\int_\infty^t\nu(t-t')\mathbf{A}^{(4)}(t,t')dt'\right], \tag{18}$$

where the "memory" functions μ and ν are given by

$$\mu(t-t')=\frac{8}{\lambda}\sum_{\alpha,\text{odd}}\exp[-\pi^2\alpha^2(t-t')/\lambda], \tag{19}$$

$$\nu(t-t')=\frac{16}{\pi^2\lambda}\sum_{\alpha,\text{odd}}\alpha^{-2}\exp[-\pi^2\alpha^2(t-t')/\lambda] \tag{20}$$

and where $\mathbf{A}^{(2)}$ and $\mathbf{A}^{(4)}$ are averages calculated from

$$\mathbf{A}^{(2)}=\frac{1}{4\pi}\int\frac{\mathbf{uu}}{(1+\gamma^{(0)}:\mathbf{uu})^{3/2}}\,d\mathbf{u}, \tag{21}$$

$$\mathbf{A}^{(4)}=\frac{1}{4\pi}\int\frac{\mathbf{uuuu}}{(1+\gamma^{(0)}:\mathbf{uu})^{3/2}}\,d\mathbf{u}. \tag{22}$$

In these equations, $\gamma^{(0)}$ is the relative strain tensor.[13] In the first stage of the flow, the stress tensor is found by evaluating the right-hand side of Eq. (18). During recovery $\tau_{xy}=0$, and the shear rate is found by solving for κ in Eq. (18). If only the xy components of the stress tensor are of interest, Eqs. (21) and (22) can be further simplified[3] to give

$$A_{xy}^{(2)}=\frac{1}{2\Gamma}\int_0^1[1+g^{-1}(\Gamma^2x^2-1)]dx, \tag{23}$$

$$B_{xy}^{(2)}=\frac{\lambda\dot{\gamma}_{xy}}{4\Gamma^2}\int_0^1\{1+g^{-3}[(3\Gamma^6+8\Gamma^4)x^6-(7\Gamma^4+8\Gamma^2)x^4$$
$$+5\Gamma^2x^2-1]\}dx, \tag{24}$$

where

$$\mathbf{B}^{(2)}=\tfrac{1}{2}(\lambda\dot{\gamma}:\mathbf{A}^{(4)}), \tag{25}$$

$$g=[(\Gamma^4+4\Gamma^2)x^4-2\Gamma^2x^2+1]^{1/2}, \tag{26}$$

and

$$\Gamma(t,t')=-\gamma_{xy}(t,t')=\int_{t'}^t\dot{\gamma}_{xy}(t'')dt''. \tag{27}$$

The stress tensor is therefore determined from

$$\tau_{xy}=-k_BTnN\left[\int_{-\infty}^t\mu(t-t')(A_{xy}^{(2)})_\Gamma\,dt'\right.$$
$$\left.+\epsilon_l\int_{-\infty}^t\nu(t-t')(B_{xy}^{(2)})_\Gamma\,dt'\right]. \tag{28}$$

To ensure accurate results, we employ a predictor–corrector scheme and a Romberg integration method for the integrals appearing in Eq. (28).

RESULTS

We begin this section by illustrating how the recoil numerical experiment is prepared. As mentioned earlier, a steady state must be developed before the recovery calculation can proceed. Figure 7 shows the shear viscosity as a function of time, for inception of shear flow, determined from a stochastic simulation. The results shown in Fig. 7 correspond to $\lambda\dot{\gamma}_0=100$ and $\epsilon_l=0.1$. Bird *et al.*[3] have found that link-tension coefficients with values between 0.1 and 0.5 can provide a reasonable description of experimental data.[3] From a numerical point of view, calculations become more difficult as ϵ_l becomes smaller. The overshoot which the curve exhibits for high shear rates is consistent with experiment.[13] Note, however, that the stress tensor has a nonzero value at $t=0^+$. This sudden jump at $t=0$ disappears for $\epsilon_l=0$. In the past, Bird *et al.*[21] have suggested that it could be

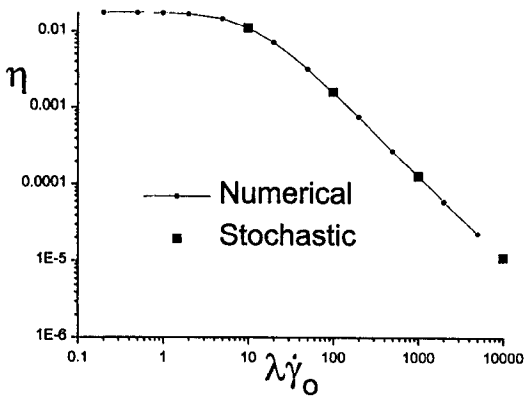

FIG. 8. Steady-state shear viscosity η for $\lambda\dot{\gamma}_0$ for $\epsilon_l=0.1$. The solid line shows results of calculations performed by conventional numerical techniques. The solid squares show results of stochastic simulations.

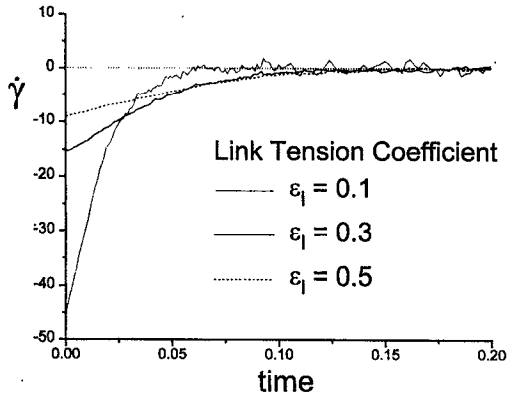

FIG. 10. Shear rate $\dot{\gamma}(t)$ during constrained recovery after shear flow for $\lambda\dot{\gamma}_0=10$. The lines show results of stochastic simulations for different values of the link-tension coefficient ϵ_l.

a consequence of assuming that a linear velocity profile develops instantly and of employing Kramer's chains in the theoretical development of their model.

For shear flows, the viscosity function was calculated using both the conventional numerical method and stochastic simulations. Figure 8 shows the viscosity as a function of shear rate for $\epsilon_l=0.1$. The circles correspond to numerical results; the filled squares depict stochastic results. Figure 9 shows the ultimate recoil after steady shear flow as a function of shear rate calculated using both methods, also for $\epsilon_l=0.1$. If ϵ_l is increased, the viscosity curve is shifted upwards.[3,21] As shown in Figs. 10 and 11, the ultimate recovery decreases when ϵ_l is increased.

As seen in Figs. 8 and 9, the results obtained by the two methods of solution are in excellent agreement. We believe, however, that stochastic simulations have several advantages over conventional numerical integrations. The first of these is the simplicity with which stochastic simulations are implemented. The necessary codes are short and simple, in contrast to the codes for the numerical solutions. The second advantage is the physical insight into the problem that is gained by a stochastic approach. The third is the efficiency of the algorithm. At very low shear rates, conventional numerical techniques are faster than stochastic methods. However, as the shear rate is increased, the latter becomes superior. This is because for conventional numerical techniques, the required computational time scales as the square of the inverse time step; for stochastic simulations, it scales only as the inverse time step. Furthermore, in the stochastic simulations, the size of the time step required to avoid instabilities decreases rapidly as the shear rate increases; if the time step is too large during recovery, the simulations will lead to incorrect results.

The calculations presented here reveal a particularly interesting feature of the Curtiss–Bird model. As shown in Fig. 9, when plotted as a function of shear rate, the recovery curve exhibits a clear maximum. The third term in Eq. (5) is responsible for the maximum; Fig. 12 shows recovery curves as a function of shear rate for different values of the link-tension coefficient. As ϵ_l decreases, the maximum in the recovery curves is shifted towards higher values of $\lambda\dot{\gamma}_0$ and higher values of $-\gamma_\infty$. For $\epsilon_l=0$, there is no maximum, but

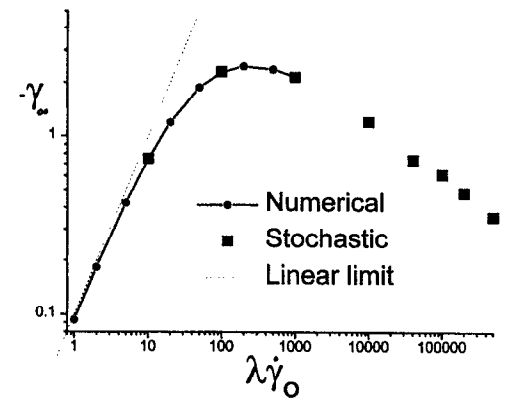

FIG. 9. Ultimate recoil after shear flow $-\gamma_\infty$ for $\epsilon_l=0.1$. The solid line shows results of numerical calculations using conventional techniques. The solid squares show results of stochastic simulations.

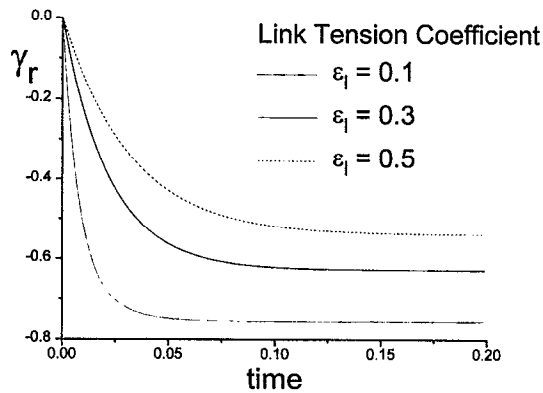

FIG. 11. Displacement $\gamma_r(t)$ during constrained recovery after shear flow for $\lambda\dot{\gamma}_0=10$. The lines show results of stochastic simulations for different values of the link-tension coefficient ϵ_l.

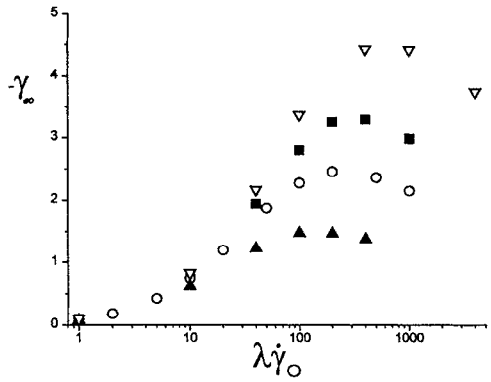

FIG. 12. Ultimate recovery for different values of the link tension coefficient ϵ_l. (Open triangles) ϵ_l=0.02; (filled squares) ϵ_l=0.05; (open circles) ϵ_l=0.1; and (filled triangles) ϵ_l=0.3. Note how the maximum is shifted upwards and right as ϵ_l is decreased. For ϵ_l=0, the maximum disappears.

the amount of recovery is largely overpredicted by the theory.

For small values of ϵ_l, the shear stress predicted by the CBM (or the Doi–Edwards model) is a nonmonotonic function of the shear rate. For sufficiently large values of ϵ_l, however, the shear stress becomes a monotonic function of shear rate.[6] We have performed calculations of recovery for values of ϵ_l of up to 0.5, which corresponds to a monotonic shear stress; all of the calculated curves (see Fig. 12) exhibit a maximum. Furthermore, note that the maximum in the recovery curve disappears as the link-tension coefficient decreases. The nonmonotonic nature of the shear stress is therefore unlikely to be responsible for the maximum observed in the recovery curve.

The magnitude of the ultimate recovery after shear flow is largely dictated by both the initial value of the shear rate $\dot{\gamma}(t_0^+)$ during recovery and the rate of change of the shear rate, also at $t=t_0^+$. These two quantities depend on the initial steady-state shear rate $\dot{\gamma}_0$. Figure 13(a) shows the time-dependent shear rate $\dot{\gamma}(t)$ during recovery for different values of the initial shear rate $\lambda\dot{\gamma}_0$ and for constant ϵ_l=0.3. As $\lambda\dot{\gamma}_0$ is increased, both the initial value of $\dot{\gamma}(t)$ and its initial slope also increase. Figure 13(b) shows similar results for $\lambda\dot{\gamma}_0$=65 and 400; these two values yield almost identical amounts of recovery, but are located on opposite sides of the maximum in Fig. 9. The two shaded regions in Fig. 9 illustrate the amount of recovery that is gained by having increased the initial value of $\dot{\gamma}(t)$ in going from $\lambda\dot{\gamma}_0$=65 to 400, and the amount of recoil that is lost by having gone over the maximum. The initial value of the shear rate is given by $\eta_\Omega/\dot{\gamma}_0\epsilon\eta_\epsilon$, where η_Ω and η_ϵ are the elastic and the viscous contributions to the viscosity,[8] respectively. Figure 14 shows $[\dot{\gamma}(t_0^+)]$ as a function of $\lambda\dot{\gamma}_0$; as expected, $\dot{\gamma}(t_0^+)$ increases monotonously. Figure 15 shows the time τ required for $\dot{\gamma}(t)$ to reach half of its initial value as a function of $\lambda\dot{\gamma}_0$; τ can be viewed as a characteristic relaxation time for the initial recovery of the melt. Figure 15 exhibits a clear change of slope at around $\lambda\dot{\gamma}_0\approx$100, which is actually responsible for the maximum in $-\gamma_\infty$. For moderate shear rates (but above the linear viscoelastic regime), τ increases with $\dot{\gamma}_0$; for shear

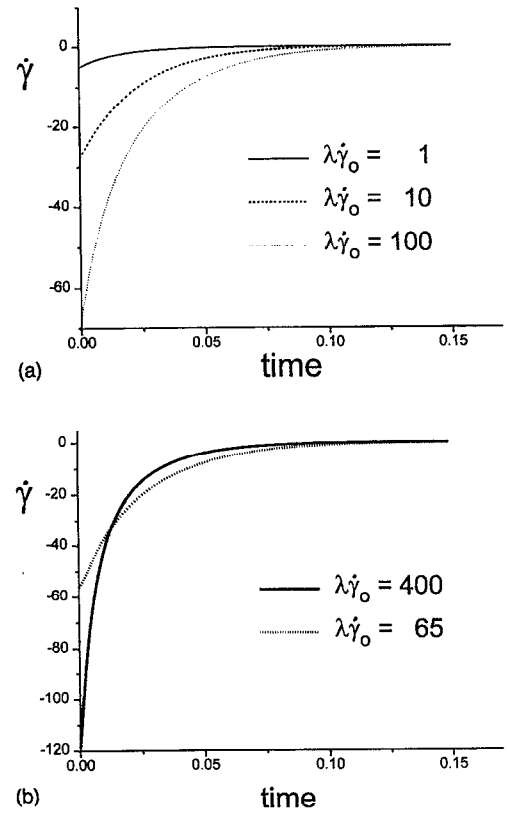

FIG. 13. (a) Time-dependent shear rates during recovery for different initial shear rates, all with shear rates lower than those where the maximum recovery is observed. (b) Time-dependent shear rates during recovery for different initial shear rates. The two shear rates have almost the same ultimate recovery value, but they are located on opposite sides of the maximum recovery.

rates above the maximum, τ decreases with $\dot{\gamma}_0$, thereby leading to a decrease of the ultimate recovery.

At this point, we do not know if such a maximum is physical. It is, however, important to emphasize possible violations of the assumptions implicit in the theory. One of the assumptions is that the velocity profile is linear during recoil; this is not the case at high shear rates (the deformation is nonuniform in this regime[22,23]). Furthermore, the alignment

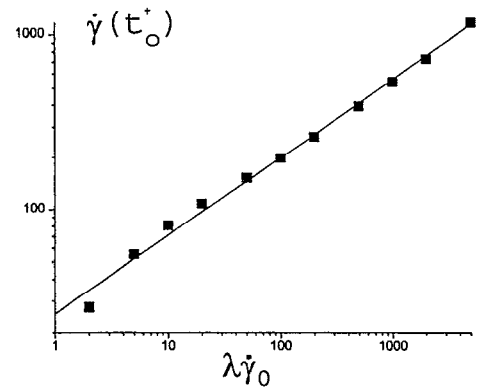

FIG. 14. Initial shear rate immediately after the onset of recovery as a function of initial shear rate.

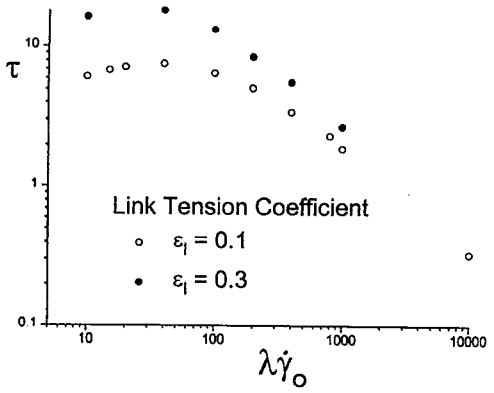

FIG. 15. Characteristic relaxation time for initial recovery as a function of initial shear rate.

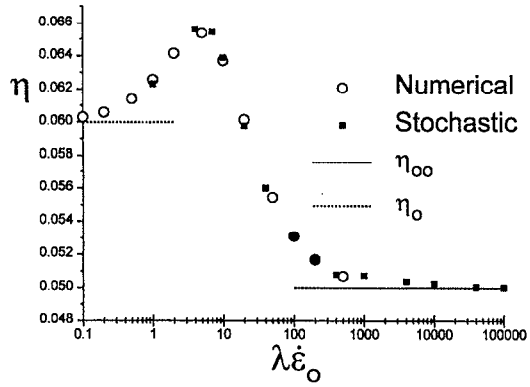

FIG. 17. Elongational viscosity $\bar{\eta}$ for $\epsilon_l=0.3$. The open circles show numerical results by Saab *et al.* (Ref. 5). The solid squares show results of our stochastic simulations. The dashed lines indicate the expected asymptotic value of the viscosity (Ref. 5) at both low and high elongational rates.

of the molecules could also be in conflict with the CBM, since part of the melt would no longer be entangled. Note that the CBM assumes that polymers are above their critical molecular weight M_e for entanglement. Bird *et al.*[8] have shown that for $M_w<M_e$, their model leads to incorrect results.

Last, we do not know whether it is physically feasible to shear at $\lambda\dot{\gamma}>200$ without changing the molecular weight of the melt.

Figure 16 shows the unsteady state elongational viscosity for $\lambda\dot{\epsilon}=10$ *and* $\epsilon_l=0.3$ determined from a stochastic simulation. As for the shear flows, a nonzero stress tensor is obtained at zero time.

Figure 17 shows the steady state elongational viscosity as a function of elongational rate for $\epsilon_l=0.3$. The circles show results of numerical calculations by Bird *et al.*[5] The filled squares depict results of our stochastic calculations. As for the case of shear flows, agreement between standard numerical calculations and stochastic calculations is excellent. Note, however, that the numerical method becomes too intensive even before an asymptotic value for the viscosity is attained; the stochastic method is able to generate reliable results over several additional orders of magnitude.

Figures 18 and 19 show the two functions $\dot{\epsilon}(t)$ and $\epsilon(t)$ for $\lambda\dot{\epsilon}_0=10$, and for three different values of the link-tension coefficient. The ultimate recoil is seen to increase with increasing link-tension coefficient. Such an increase was expected, since the elongational viscosity becomes higher for increasing ϵ_l.

Figure 20 shows the ultimate free recovery after elongational flow as a function of elongational rate. In contrast to constrained recovery after shear flow, the elongational recovery does not go through a maximum, but it reaches an asymptotic value at around $\lambda\dot{\epsilon}_0=100$.

CONCLUSIONS

We have calculated the constrained recoil after steady shear flow for a monodisperse polymer melt using the Curtiss–Bird model. The calculations were done using two different methods of solution, i.e., a conventional numerical integration method and a newer stochastic simulation method. The latter has proven to be superior in several respects. It is more flexible than conventional numerical techniques, thereby allowing easy treatment of more complex flows. Second, at high shear rates, it is faster by up to an order of magnitude. For polydisperse melts, we expect the

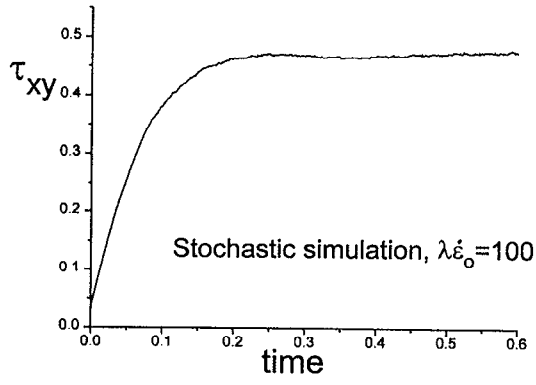

FIG. 16. Elongational stress after inception of elongational flow. The line shows results of stochastic simulations for $\lambda\dot{\epsilon}_0=100$ and $\epsilon_l=0.3$.

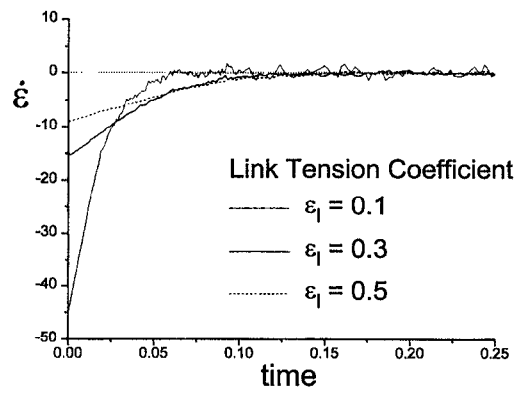

FIG. 18. Elongation rate $\dot{\epsilon}(t)$ during free recovery after elongational flow for different values of the link-tension coefficient ϵ_l.

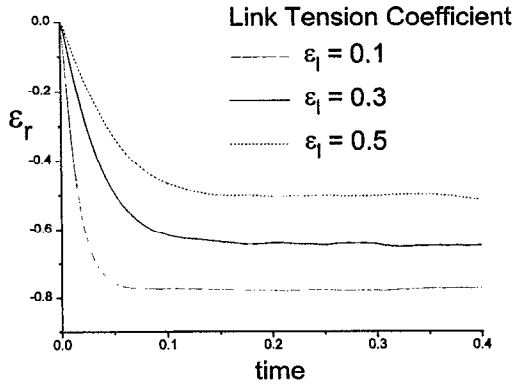

FIG. 19. Displacement ϵ_r during free recovery after elongational flow for different values of the link-tension coefficient ϵ_l.

stochastic technique to be even more advantageous, since for every additional species in the system, the corresponding code will only need to run approximately 1% longer. In contrast, conventional numerical techniques require one additional integration for each species in the system. Furthermore, the presence of sharp gradients will require small time steps which can be handled more efficiently within the framework of a stochastic simulation than within that of conventional numerical techniques.

During this work, we have found that the recovery after shear flow $-\gamma_\infty$ exhibits a maximum as a function of $\lambda\dot{\gamma}_0$ (Fig. 9). Interestingly, the maximum is only found for constrained recovery after shear flow, and not for free recovery after elongational flow. The maximum disappears when the link-tension coefficient is set equal to 0; it arises from viscous contributions to the stress tensor and we attribute it to a dramatic change in the characteristic relaxation time for initial recovery at relatively high values of $\lambda\dot{\gamma}_0$.

At this point, we are not certain that this maximum would be physically obtainable since it occurs at relatively high shear rates ($\lambda\dot{\gamma}_0 \approx 200$). Unfortunately, available experimental data for constrained recovery after shear flow have only been measured for highly polydisperse melts;[22] our attempts to describe these data with the monodisperse version

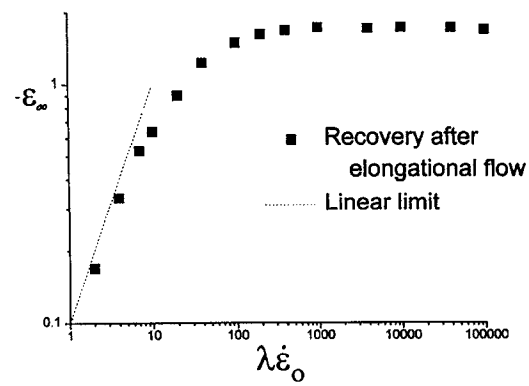

FIG. 20. Ultimate recovery $-\epsilon_\infty$ after elongational flow. The symbols show results of stochastic simulations for $\epsilon_l = 0.3$.

of the Curtiss–Bird model have met with very limited success. Previous studies of quasimonodisperse, intermediate-molecular-weight melts under shear flow suggest that λ is on the order of several seconds.[3] Such values would indicate that the maximum in the recovery curves should occur for $\dot{\gamma}_0$ on the order of hundreds of seconds; it should therefore be measurable in the laboratory.

Before drawing any conclusions about the physical significance of our results for recovery, it is therefore imperative to take into account the effects of polydispersity. It is plausible that by taking polydispersity into account the maximum in the recovery curve could disappear or, alternatively, it could be accentuated. Studies of recovery for polydisperse melts are under way in our laboratory and will be presented in a forthcoming publication.

ACKNOWLEDGMENTS

The authors are grateful to the National Science Foundation for financial support. One of us (JJdP) is also grateful to the Camille and Henry Dreyfus foundation for a New Faculty Award. Some of the calculations presented in this work were performed at the Pittsburgh Supercomputing Center and on a RS-6000 workstation awarded to us by the IBM Corporation.

APPENDIX

A reflection can arise in two different ways during a given time step. If $s_{i+1} \notin [0,1]$, the reflection was observed. If $s_{i+1} \in [0,1]$, but $P > R$, then an overseen reflection took place. In both cases, the last reflection time $t_r \in]t, t+\Delta t[$ is determined by a bisection procedure; a time *step is then* taken for $\mathbf{u}$ (starting from a random value) over the remainder of the original time step, i.e., from t_r to $t+\Delta t$. In what follows, we describe the bisection method. Note that the accuracy of the stochastic integration scheme will still be of order Δt. However, the extrapolation to zero time step will be facilitated significantly by reducing the prefactor of the time-step dependence.

Both observed and overseen reflections can be treated on the same basis by taking advantage of the reflection principle of the Wiener process and reflecting s_{i+1} over the boundary in case of an overseen reflection.[17,18]

At time t, $s_i \in [0,1]$, and $s_{i+1} \notin [0,1]$ at time $t+\Delta t$. This is a Wiener process, bounded at both ends; s must necessarily cross the boundary B at least once during this time step. The bisection method is used to "decide" whether the last boundary crossing occurred in the first or in the last half of the time step. To do so, we calculate $s_{i+(1/2)} = (s_{i+1} + s_i)/2 + \frac{1}{2}\sqrt{(2\Delta t)/\lambda}\,\mathbf{W}_i$ at time $t+\frac{1}{2}\Delta t$.[17]

There are now two possibilities, namely, $s_{i+(1/2)} \in [0,1]$ or $s_{i+1/2} \notin [0,1]$. If $s_{i+1/2} \in [0,1]$, then a crossing occurred between $t+\frac{1}{2}\Delta t$ and $t+\Delta t$; the bisection is therefore continued on the second half of the interval. In the second case, a crossing did occur in the first half of the interval, but one or more additional boundary crossings might also have occurred in the second interval. To decide whether this is the case or not, Eq. (18) is used with $\frac{1}{2}\Delta t$ instead of Δt and $s_{i+(1+2)}$ instead of S_i. If P is larger than a random number, then a crossing did occur; otherwise no crossings occurred.

This entire procedure can now be repeated until the desired precision is achieved. We used four bisection steps throughout our work.

An obvious way of improving the bisection method as described above would be to find the distribution function for the last crossover time, given the aforementioned double bounded Wiener process. This function can be found from the distribution of the first cross over time, which could be derived from knowledge of the Wiener process.

[1] A. S. Lodge, R. C. Armstrong, M. H. Wagner, and H. H. Winter, Pure Appl. Chem. **54**, 1349 (1982).
[2] M. Doi and S. F. Edwards, *The Theory of Polymer Dynamics* (Clarendon, Oxford, 1986).
[3] R. B. Bird, C. F. Curtiss, O. Hassager, and R. A. Armstrong, *Dynamics of Polymeric Liquids*, 2nd ed. (Wiley, New York, 1987), Vol. 2.
[4] R. J. J. Jongschaap and B. J. Geurts, Rolduc Polymer Meeting 2, 1987.
[5] R. B. Bird, H. H. Saab, and C. F. Curtiss, J. Phys. Chem. **86**, 1102 (1982).
[6] H. H. Saab, R. B. Bird, and C. F. Curtiss, J. Chem. Phys. **77**, 4758 (1982).
[7] J. D. Schieber, C. F. Curtiss, and R. B. Bird, Ind. Eng. Chem. Fundam. **25**, 471 (1986).
[8] J. D. Schieber, J. Chem. Phys. **87**, 4928 (1987).
[9] H. C. Öttinger, J. Chem. Phys. **91**, 6455 (1989).
[10] H. C. Öttinger, presentation at the 198th ACS National Meeting in Miami Beach, 1989 (preprint).
[11] H. C. Öttinger, J. Chem. Phys. **92**, 4540 (1989).
[12] T. W. Liu, J. Chem. Phys. **90**, 5826 (1989).
[13] R. B. Bird, O. Hassager, and R. C. Armstrong, *Dynamics of Polymeric Liquids*, 2nd ed. (Wiley, New York, 1987), Vol. 1.
[14] A. Lodge, *Elastic Liquids* (Academic, New York, 1964).
[15] C. W. Gardiner, *Handbook of Stochastic Methods* (Springer, Berlin, 1990).
[16] P. E. Kloeden and E. Platen, *Numerical Solutions to Stochastic Differential Equations* (Springer, Berlin, 1992).
[17] P. G. Hoel, S. C. Port, and C. J. Stone, *An Introduction to Stochastic Processes* (Houghton–Mifflin, Boston, 1972).
[18] S. Karlin and H. M. Taylor, *A First Course in Stochastic Processes*, 3rd ed. (Academic, New York, 1975), Vol. 2.
[19] J. Honerkamp and R. Seitz, J. Chem. Phys. **87**, 3120 (1987).
[20] W. Strittmatter, J. Stat. Phys. (to be published).
[21] R. B. Bird, H. H. Saab, and C. F. Curtiss, J. Chem. Phys. **77**, 4747 (1982).
[22] H. M. Laun, Rheol. Acta. **21**, 464 (1982).
[23] F. Nazem and M. G. Hansen, J. Appl. Poly. Sci. **20**, 1355 (1976).